Ceramics International 47 (2021) 5415–5422

Contents lists available at ScienceDirect

Ceramics International

journal homepage: www.elsevier.com/locate/ceramint

Carbon combustion synthesis of Janus-like particles of magnetoelectric cobalt ferrite and barium titanate

C. Trevino De Leo [a], G.C. Dannangoda [a], M.A. Hobosyan [a], J.T. Held [b], F. Safi Samghabadi [c], M. Khodadadi [c], D. Litvinov [c], K.A. Mkhoyan [b], K.S. Martirosyan [a,*]

[a] Department of Physics and Astronomy, University of Texas Rio Grande Valley, Brownsville, TX, 78520, USA
[b] Department of Chemical Engineering and Materials Science, University of Minnesota, Minneapolis, MN, 55455, USA
[c] Materials Science & Engineering and Electrical & Computer Engineering, University of Houston, Houston, TX, 77204, USA

ABSTRACT

Carbon combustion synthesis of oxides was applied for quick and energy efficient production of multiferroic composite of cobalt ferrite and barium titanate to form Janus-like particles matrix structure. The exothermic oxidation of carbon nanoparticles with an average size of 5 nm and a specific surface area of 110 m^2/g generates a self-propagating thermal wave with peak temperature of up to 1000 °C. The thermal front rapidly propagates through the mixture of solid reactants (magnetic-$CoFe_2O_4$ and ferroelectric-$BaTiO_3$) and results in localized hot-spot sintering of magneto-electric phases to form a nanocomposite structure. Carbon is not incorporated in the product and is emitted as a gaseous CO_2. Existence of discrete $CoFe_2O_4$ and $BaTiO_3$phases in the composites nanostructures was confirmed using X-ray powder diffraction along with SEM and TEM analysis. We estimated the activation energy for the combustion synthesis of Janus-like particles to be 112 ± 3.3 kJ/mol, indicating that the barium titanate and cobalt ferrite presence decrease the activation energy barrier of carbon oxidation and facilitate the ignition process of the combustion synthesis. We observe that the as-synthesized samples show magnetoelectric coupling on multiferroic cobalt ferrite–barium titanate ceramic composites.

1. Introduction

The $BaTiO_3$–$CoFe_2O_4$ magnetoelectric composites are of great technological interest for their potential applications in microwave devices, antennae, sensors, transducers, data storage, controlled release of anti-HIV drug delivery and Alzheimer's, Parkinson's disease treatment [1–3]. These composites are artificial multiferroics as they exhibit two distinct ferroic properties, ferromagnetism of $CoFe_2O_4$ and ferroelectricity of $BaTiO_3$, which are coupled via physical interaction between the $CoFe_2O_4$ and $BaTiO_3$ phases [4].

$CoFe_2O_4$ is a magnetostrictive material, in which magnetostriction strongly depends on its cation distribution [3], while $BaTiO_3$ exhibits piezoelectric properties, in which spontaneous electric polarization arises from the displacement of Ti^{4+} along the crystallographic c-axis [5]. At room temperature, $CoFe_2O_4$ has a spinel crystal structure whereas $BaTiO_3$ has perovskite structure. Physical-mechanical coupling between $CoFe_2O_4$ and $BaTiO_3$ in a composite allows to modulate the magnetization via the application of external electric field and the electric polarization via the application of external magnetic field. An applied electrical field induces stress in $BaTiO_3$, which in turn causes stress in $CoFe_2O_4$ that results in the change of cobalt ferrite magnetization. Similarly, the application of a magnetic field induces stress in $CoFe_2O_4$, which in turn causes stress in $BaTiO_3$ that results in the change of $BaTiO_3$ polarization. Since the magnetoelectric effect in a $BaTiO_3$–$CoFe_2O_4$ composite results from cross-interaction between the two phases and the interfaces between these phases can be tailored using an array of materials engineering techniques, such composites can typically be designed to exhibit stronger magnetoelectric properties than what is achievable in a single-phase multiferroic material [5–7].

Various methods to synthesize $BaTiO_3$–$CoFe_2O_4$ composites have been reported, including nanocasting [6], reductive sintering and reoxidation [7], electrospinning of nanofibers [8], embedding of $CoFe_2O_4$ nanopillars into $BaTiO_3$ matrix [5], co-precipitation and sol-gel techniques to form core-shell nanoparticles, etc. [9–13]. Of these materials, the core–shell structures typically exhibit the highest magnetoelectric (ME) coefficients [10]. While these approaches have produced a variety of $BaTiO_3$/$CoFe_2O_4$ composite structures, the formation of Janus-like particles, which have biphasic geometry of distinct compositions and properties [14–16] has not been reported in the $BaTiO_3$–$CoFe_2O_4$ system. In contrast to core-shell structures, Janus-like particles with their two chemically and structurally distinct surfaces could provide additional flexibility, for example, an option of distinct functionalizations of the two surfaces for applications in drug delivery.

In this report, we utilized a highly exothermic method called Carbon

---

* Corresponding author.
E-mail address: karen.martirosyan@utrgv.edu (K.S. Martirosyan).

https://doi.org/10.1016/j.ceramint.2020.10.123
Received 20 September 2020; Received in revised form 16 October 2020; Accepted 16 October 2020

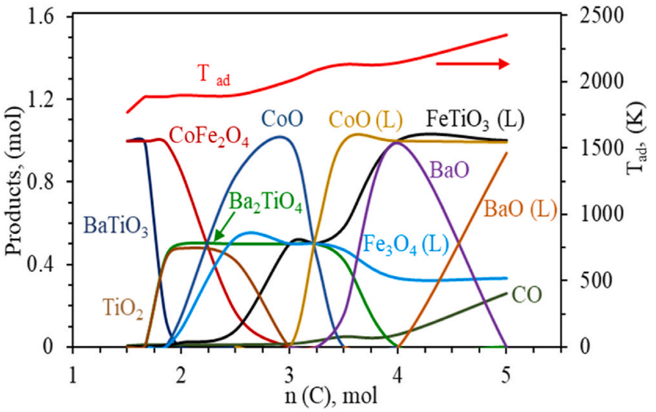

Fig. 1. Adiabatic temperature of combustion and product composition dependence on the amount of carbon concentration in the system $BaTiO_3$–$CoFe_2O_4$-n ($C + O_2$) by CCSO.

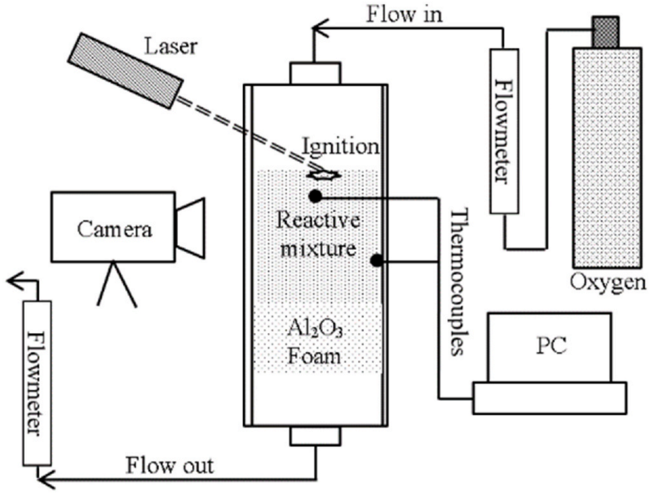

Fig. 2. Schematics of the experimental setup, for carbon combustion synthesis of $BaTiO_3$–$CoFe_2O_4$-10 wt % C.

Combustion Synthesis of Oxides (CCSO) [17–22] to produce $BaTiO_3$–$CoFe_2O_4$ matrix structure with Janus-like particles. In CCSO, carbon nano powder is used as a fuel and oxygen as an oxidizer producing heat by following reaction $C + O_2 = CO_2$ with $\Delta H^{298}_{CO_2} = -393.5$ kJ/mol. After igniting a powder mixture of initial mixture with carbon nano particles generates a thermal reaction front with temperatures at ~1000 °C that propagates at a velocity of 0.1–4 mm/s through the solid reactant mixture. The heat of the carbon oxidation (-ΔH) is sufficient to sinter $BaTiO_3$ and $CoFe_2O_4$ particles to produce Janus-like particles with matrix structures. In general, this method can also be applied for simple and energy efficient production of nanocomposite materials from a variety of complex oxides. It is significantly simpler, faster, and more energy efficient as compared to calcination processes that require prolong annealing (hours) at high temperatures.

1.1. Thermodynamic analysis

Thermodynamic analysis of the CCSO system $BaTiO_3$–$CoFe_2O_4$-n($C + O_2$) is critical to evaluate the energetic capacity of the system, prediction of the adiabatic temperature, condensed and liquid phase concentrations, which will determine the possibility of particle sintering and combustion front propagation. The thermodynamic estimation of the equilibrium composition of multicomponent multiphase systems requires minimization of the thermodynamic free energy (G) subject to mass and energy balances [23]. The thermodynamic calculations were made using "Thermo" software [24], which includes database with thermochemical properties of approximately 3000 compounds.

The composition of the equilibrium products and adiabatic temperature can be determined by minimizing the thermodynamic potential. For a system with N(g) gas and N(s) solid number of components, at constant pressure, the concentrations of equilibrium phases can be expressed as:

$$F(\{n_k\},\ \{n_s\}) = \sum_{k=1}^{N^{(g)}} n_k\left(ln\frac{p_k}{p}+G_k\right) + \sum_{l=1}^{N^{(s)}} n_l G_l \tag{1}$$

where p_k is the partial pressure of the k'th gas-phase component, while n_l and G_l are the number of moles and molar Gibbs free energy of components. The adiabatic combustion temperature, T_c^{ad}, is determined by total energy balance:

$$\sum_{i=1}^{N_0} H_i(T_0) = \sum_{k=1}^{N_{(g)}} n_k H_k\left(T_c^{ad}\right) + \sum_{l=1}^{N_{(s)}} n_l H_l\left(T_c^{ad}\right) \tag{2}$$

where the enthalpy of each component is

$$H_i(T) = \delta H^0_{f,i} + \int_{T_0}^{T} c_{p,i} dT + \sum \delta H_{s,i} \tag{3}$$

and $\delta H^0_{f,i}$ is the heat of formation at 1 atm and reference temperature T_0, $c_{p,i}$ is the heat capacity, and $\delta H_{s,i}$ is the heat of s'th phase transition for components [25].

The prediction of the adiabatic interaction temperature and equilibrium product composition for the $BaTiO_3$–$CoFe_2O_4$-nC system combustion in oxygen, includes estimation of multiple phases at various temperatures. Fig. 1 shows the dependence of the adiabatic temperature and equilibrium concentration of condensed, liquid and gaseous phases during the exothermic reaction in system $BaTiO_3$–$CoFe_2O_4$-n(C) in O_2, where n is the molar concentration of carbon in the $BaTiO_3$–$CoFe_2O_4$ mixture. The liquid components have (L) next to the chemical composition in the graph, otherwise the products are solid or gas (CO and CO_2 are the only gaseous components, the CO_2 concentration is not shown). Initially, when the carbon molar concentration is 1.5 (corresponding to 3.7 wt % carbon in the mixture), the combustion temperature is 1770 K, and the $BaTiO_3$ and $CoFe_2O_4$ play the role of thermal absorbers. However, when the molar concentration of carbon is increased to 1.7 mol (or 4.2 wt %), the $BaTiO_3$ starts to decompose into Ba_2TiO_4 and TiO_2 at temperature ~1890 K. The decomposition of $BaTiO_3$ into Ba_2TiO_4 and TiO_2 is completed at n = 2 mol (or 4.9 wt %) carbon concentration. At this concentration, the temperature is ~1900 K and all combustion products are solid, in addition to gaseous CO_2 (not shown).

However, this is the starting point, when the $CoFe_2O_4$ also starts to decompose into solid CoO and liquid Fe_3O_4. Thus, this is the minimum concentration (4.9 wt %) of carbon that we might expect any liquid phase in the system. When the carbon concentration is increased, some part of liquid Fe_3O_4 reacts to TiO_2 forming the second liquid phase $FeTiO_3$ (L), until the TiO_2 is completely consumed at around 3 mol (7.1 wt %), of carbon, after which Ba_2TiO_4 starts to react with liquid Fe_3O_4, increasing the amount of liquid $FeTiO_3$ in the products. In addition, at n = 3 mol (7.1 wt % carbon) the third liquid component (liquid CoO) starts to form, when the temperature reaches 2008 K and CoO melts. Finally, at n = 4 mol (9.3 wt % carbon concentration in the system), the temperature reaches to 2145 K, and BaO also starts to melt, generating the fourth and final liquid phase BaO (L). Thus, when the carbon concentration reaches 5 mol (11.4 wt % carbon), the temperature reaches 2353 K and we have all products (CoO, $FeTiO_3$, BaO, Fe_3O_4) melted, in addition to gaseous CO and CO_2 (not shown). Thus, although already at 4.9 wt % of carbon concentration, the adiabatic temperature reaches to ~1900 K and liquid component (Fe_3O_4) starts to form, we have chosen

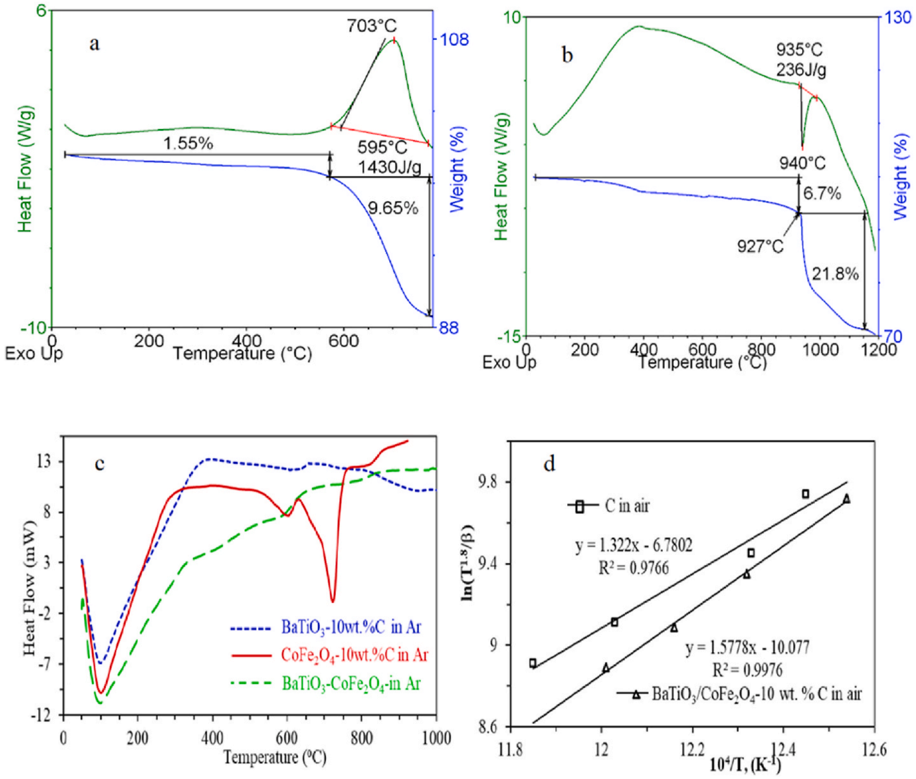

Fig. 3. (a) - DSC of $BaTiO_3$ - $CoFe_2O_4$ -10 wt % C mixture in oxygen; (b) - DSC of $BaTiO_3$ -$CoFe_2O_4$-10 wt % C mixture in inert atmosphere; (c) - DSC of $BaTiO_3$ -$CoFe_2O_4$ mixture, $BaTiO_3$-10 wt % C mixture, and $CoFe_2O_4$-10 wt % C mixture in inert atmosphere (Ar); (d) Arrhenius plot for the carbon nanoparticles combustion (square), and $BaTiO_3$–$CoFe_2O_4$-10 wt % C system combustion (triangle) at heating rates at 10–25 °C/min.

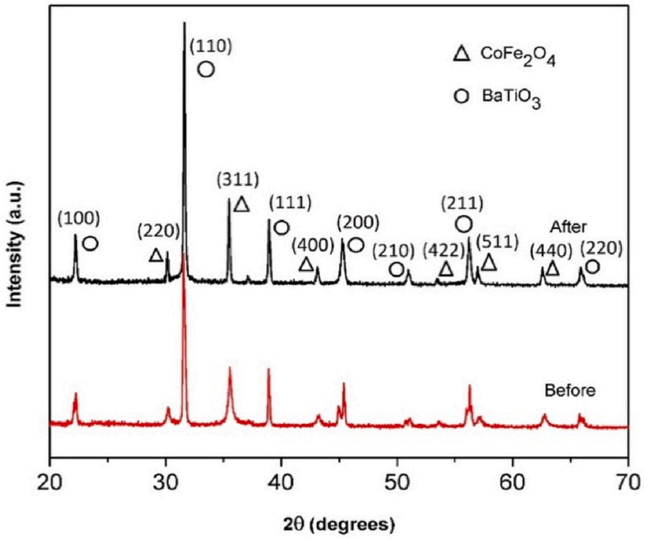

Fig. 4. XRD patterns of samples before and after combustion.

Table 1
Crystallite size calculation for the sample before and after reaction.

	Size ($BaTiO_3$), nm	Size ($CoFe_2O_4$), nm
Before	41.6	32.5
After	63	71.8

the system with 10 wt % carbon to allow more liquid components in the system (not all components will be melted due to thermal losses), and greater possibility of forming sintered particles to form Janus-like particle structures in the system $BaTiO_3$–$CoFe_2O_4$.

The reactants mixture of 200 nm $BaTiO_3$ and 30 nm $CoFe_2O_4$ nanoparticles with equal weight percentages was combined with 10 wt % carbon nanoparticles "Carbon Acetylene Black" with the average particle size of 5 nm. The reactants were mixed using roller ball milling for 3 h.

The combustion synthesis was conducted by loading the mixture with a relative density of about 0.4 into a tempered glass cylinder with a diameter of 15 mm. A schematic of the experimental system is shown in Fig. 2. The powder was placed on a porous alumina substrate with oxygen being fed through at a flow rate of 3 L/min. Thermocouples were positioned at the center of the sample and close to the cylinder wall to record the temperature variation during the combustion. To initiate the propagating temperature front, the reactant mixture was ignited by a 1.4 W blue laser.

The as-synthesized product was characterized using X-ray diffraction (XRD) by using Bruker D2 Phaser diffractometer with Cu-Kα radiation ($\lambda = 1.5406$ Å, $20 < 2\theta < 70°$) in step size of 0.02° with 0.2 s counting time per step. The average crystallite size was estimated using the Scherrer equation.

Differential Scanning Calorimeter (DSC) with a sensitivity of 0.1 mg (Q-600, TA Instruments) was used for thermo-gravimetric analysis (TGA). The measurements were carried out in air by varying the temperature from room temperature to 800 °C at 20° min^{-1}. Particle morphology, composition and size distribution analyses were performed using a JEOL 7800F field emission scanning electron microscope (SEM), equipped with an electron dispersive X-ray spectroscopy (EDX) system. Particle surface potential was measured using an atomic force microscope (AFM) equipped with conductive tips (NT-MDT SOLVER Nano).

Transmission electron microscopy (TEM) samples were prepared by crushing the nanocomposite samples under isopropanol with a mortar and pestle, followed by sonication for about 3 min. The particle suspension was then drop-cast onto holey carbon TEM grids. TEM cross-

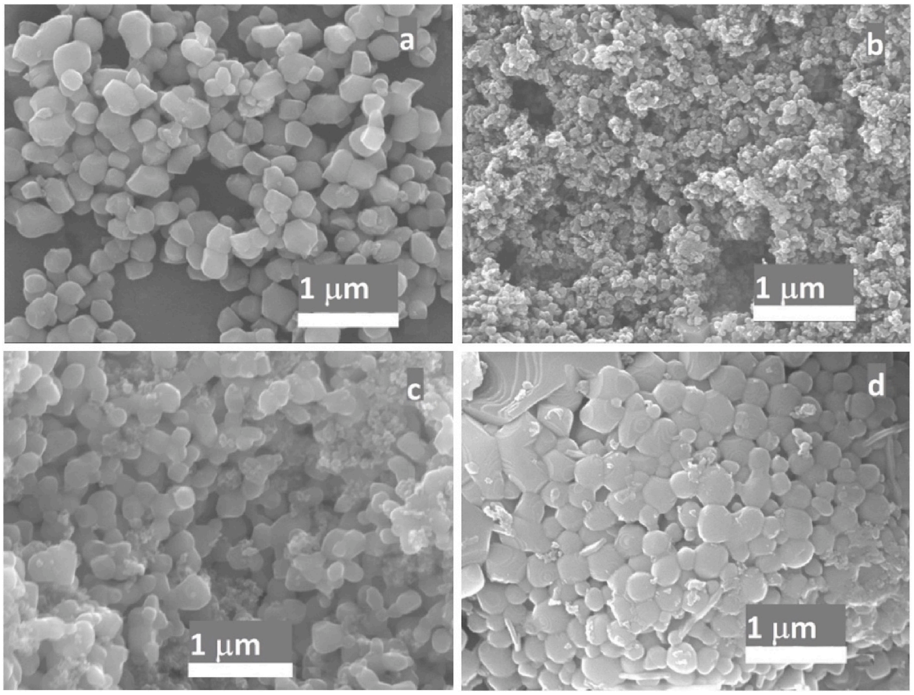

Fig. 5. SEM images of (a) - $BaTiO_3$; (b) - $CoFe_2O_4$; (c) - $BaTiO_3/CoFe_2O_4/C$ mixture before combustion; and (d) - after combustion showing formation of Janus-like particles.

sectional lamellae were prepared using FEI Helios NanoLab G4 dual-beam focused ion beam (FIB). Annular dark-field (ADF) scanning transmission electron microscopy (STEM) imaging and STEM-EDX mapping were performed on an FEI Titan 60–300 STEM equipped with a Super-X EDX spectrometer operated at 60 kV with a probe convergence angle of 25 mrad and a beam current of 125 pA.

Magnetic properties were characterized using Physical Property Measurement System (PPMS EverCool-II, Quantum Design, Inc.) equipped with the vibrating sample magnetometer (VSM) option. Saturation magnetization (M) and coercivity were obtained from the hysteresis loops at room temperature under a maximum applied field of ±90 kOe. Zero-field-cooling (ZFC) and field-cooling (FC) magnetization curves were measured in the temperature range of 10 K–400 K under the field of 100 Oe. ZFC measurements were performed by cooling down the sample from room temperature to 10 K without applying external magnetic field. After reaching 10 K, a magnetic field of 100 Oe was applied and the sample was heated to 400 K while measuring the magnetization to obtain the ZFC curve. FC curve was obtained by cooling down the sample from 400 K to 10 K while the field of 100 Oe was applied.

For ME measurements, the $BaTiO_3/CoFe_2O_4$ composites were pressed into the pellets of 10 mm diameter and 2 mm thickness. The samples were heated to 150 °C (Curie temperature of $BaTiO_3$ is ~120 °C) in a silicone oil bath followed by the application of a dc voltage of 340 V across the pellet for 15 min. The samples were removed from the oil bath and allowed to cool down to room temperature while maintaining the applied dc voltage for 15 min after removing from the oil bath. Magnetoelectric properties were measured using a custom-built magnetoelectric system similar to the one described in Refs. [26,27]. The samples were excited by an alternating magnetic field (~1 Oe, 1 kHz) and the resulting induced ac voltage was measured using lock-in technique as a function of applied DC magnetic field.

2. Results and discussion

Based on thermocouple data as the combustion wave passed through the region where the thermocouple was embedded, the maximum combustion temperature reached approximately 980 °C. The combustion product was then used for further analysis without any modification.

Thermo-gravimetric analysis and differential scanning calorimetry of the initial $BaTiO_3$–$CoFe_2O_4$-10 wt % C mixture were used to estimate the amount of absorbed humidity and observe the decomposition characteristics of the product. In all DSC graphs the initial endotherm below 200 °C is due to the absorbed moisture in the mixtures. The TGA-DSC measurements show that the combustion of mixture in air is exothermic with ignition temperature of about 580 °C and heat release of 1430 J/g presented in Fig. 3, a. The maximum heat flow was recorded around 703 °C. The initial weight decrement of 1.5 wt% from room temperature to 580 °C is attributed to adsorbed moisture. The further weight decrement of 9.65 wt% is attributed to carbon oxidation (to CO_2) as the temperature reaches 800 °C. Based on the initial carbon content in the mixture (10 wt%), it can be assumed that almost all carbon is burnt off when the temperature reaches 800 °C.

If the oxygen flow is not sufficient during CCSO, carbon might react with some of the constituents in the mixture. To analyze the behavior of the system $BaTiO_3$–$CoFe_2O_4$-10 wt % C in the absence of oxygen, the TGA-DSC was conducted in the inert atmosphere (argon, 100 mL/min flow rate with at 20° min^{-1} up to 1200 °C, Fig. 3, b). A well-formed endotherm was detected around 930 °C. The system $BaTiO_3$–$CoFe_2O_4$ without carbon (both in the air or argon) does not exhibit any endotherms, and $BaTiO_3$-10 wt % C system also does not have endotherm in argon (Fig. 3, c). However, the system $CoFe_2O_4$-10 wt % C has deep endotherm at around 700 °C in argon, as Fig. 3, c demonstrates. Thus, we conclude that the endotherm in the system $BaTiO_3$–$CoFe_2O_4$-10 wt % C is due to the interaction between $CoFe_2O_4$ and carbon, where $CoFe_2O_4$ decomposes into Co_3O_4 and Fe_3O_4 (endotherm process) and subsequently Co_3O_4 decomposes into CoO and releases oxygen, which reacts with carbon and leaves the system, causing the weight decrease as can be seen in Fig. 3, b. The reaction sequence can be given as

$$3CoFe_2O_4 \rightarrow Co_3O_4 + 2Fe_3O_4 \tag{4}$$

$$Co_3O_4 \rightarrow CoO + \frac{1}{2}O_2 \tag{5}$$

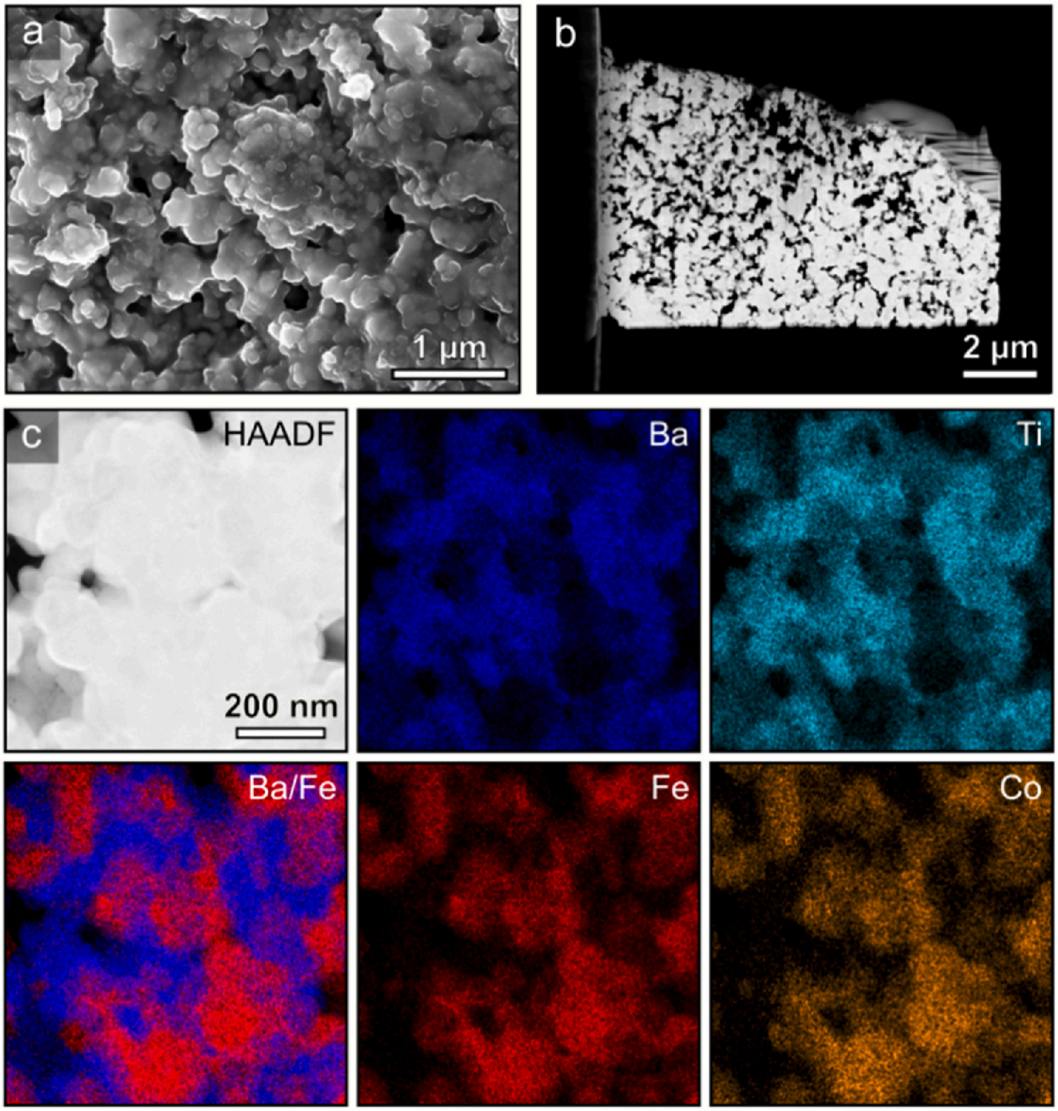

Fig. 6. Structure and composition of $BaTiO_3/CoFe_2O_4$ agglomerates after combustion. (a) - SEM image of the surface of the agglomerate; (b) - HAADF-STEM image of a cross-sectional FIB lamella taken from a region near (a); (c) - HAADF-STEM image and complementary STEM-EDX elemental maps of the same region of the cross-sectional lamella. A Ba/Fe overlaid STEM-EDX map is also shown. A 3-pixel Gaussian blur was applied to the STEM-EDX maps to aid visualization.

$$C + \frac{1}{2}O_2 \rightarrow CO \tag{6}$$

The carbon facilitates the decomposition of $CoFe_2O_4$, as without carbon we did not see any decomposition of $CoFe_2O_4$ in argon up to 1200 °C. The results suggest that the CCSO of the system $BaTiO_3$–$CoFe_2O_4$-10 wt % C should be performed in sufficient supply of oxygen, otherwise unwanted reactions (4–6) occur. In the CCSO reaction products discussed later in this section, we did not detect any Fe_3O_4 or CoO, thus, the supply of oxygen during the synthesis of Janus-like particles was sufficient to completely oxidize all the carbon in the system.

For the CCSO synthesis, we estimated the activation energy from the DSC data by using the isoconversional method suggested by Starink [28], which was shown to provide a more accurate value than the Kissinger and Ozawa methods [29,30]. The Starink method determines the activation energy from the equation:

$$ln\left\{\frac{T^{1.8}}{\beta}\right\} = \left(1.007 - 1.2 \times 10^{-5}E_a\right)\frac{E_a}{RT} + const \tag{7}$$

where E_a is the apparent activation energy (in kJ/mol), β is the heating rate in thermal analysis (in K/min), T is the peak temperature of the exothermic curve (in K), and R the universal gas constant. E_a is estimated from the slope of the graph of $\ln(\beta/T^{1.8})$ vs. $10^4/T$. We estimated the activation energy for the carbon nanoparticles oxidation from the slope of the graph (Fig. 3, d) as 131.1 ± 9.9 kJ/mol, while the activation energy for the system $BaTiO_3/CoFe_2O_4$-10 wt % C was 112 ± 3.3 kJ/mol, indicating that the $BaTiO_3/CoFe_2O_4$ particles decrease the activation energy barrier for carbon combustion and facilitate the ignition process of the combustion.

The XRD analysis (Fig. 4) shows that both the initial and final products are comprised of tetragonal $BaTiO_3$ and cubic $CoFe_2O_4$ phases without any trace of secondary and carbide phases in the composites. This indicates that formation of titanium carbide is not developed under oxygen environment and the reaction of formation of CO_2 by combustion of carbon and oxygen is the main source of exothermic reaction. Close similarity between the XRD spectra of initial and final products suggests that $BaTiO_3$ and $CoFe_2O_4$ phases are mostly preserved during combustion process and the carbon is not incorporated in the product and it is emitted as a gaseous CO_2.

However, after combustion, the peaks appear to be sharper and with higher intensity. It can be concluded that even without using any subsequent heat treatment to induce crystallinity, crystallite size and

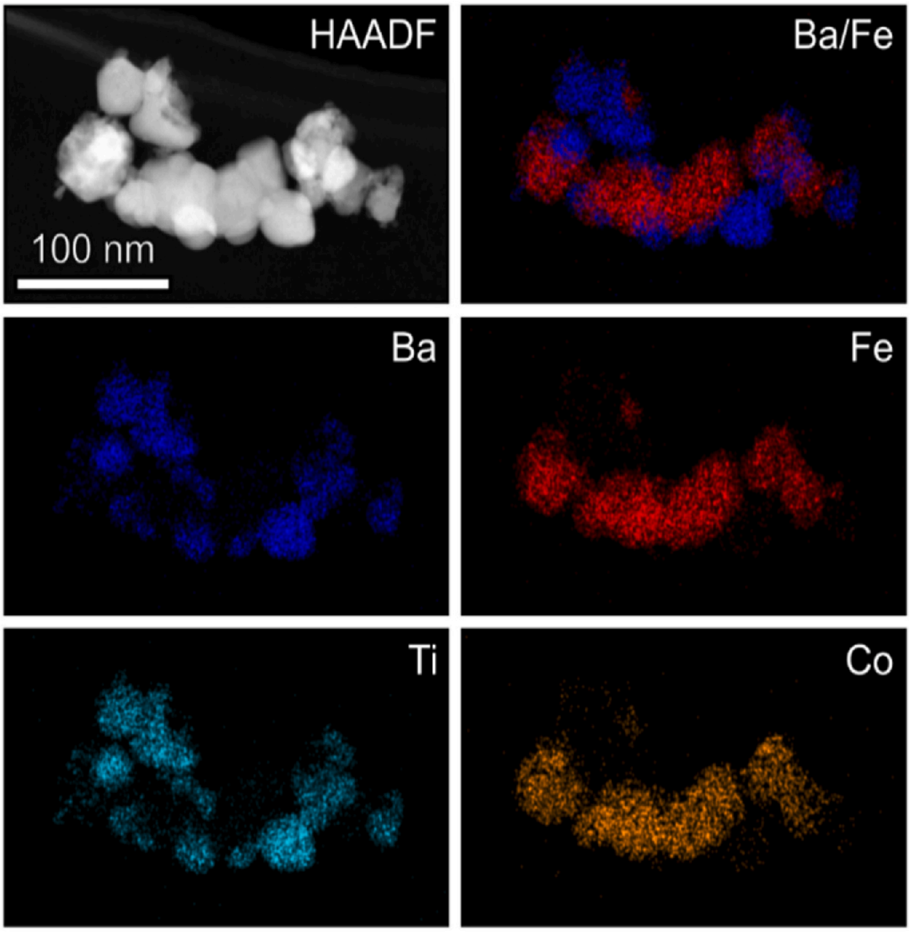

Fig. 7. HAADF-STEM image and complementary STEM-EDX elemental maps of a $BaTiO_3/CoFe_2O_4$ agglomerate. A Ba/Fe overlaid STEM-EDX elemental map is also shown. A 3-pixel Gaussian blur was applied to the STEM-EDX maps to aid visualization.

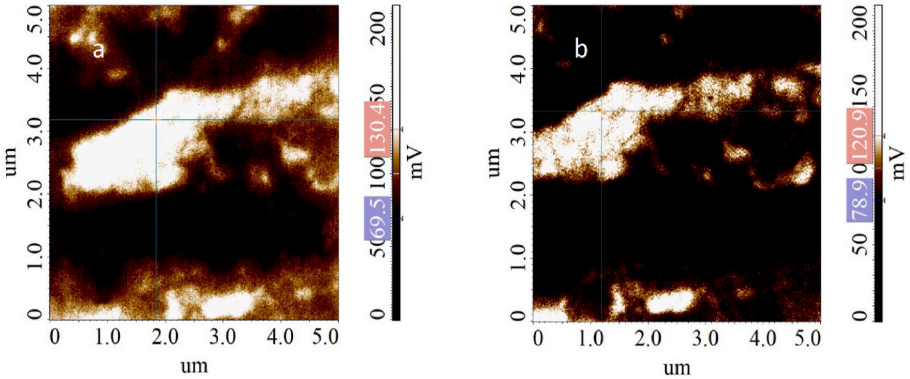

Fig. 8. (a) - AFM surface potential measurements without magnetic field; and (b) - under magnetic field of 150 G, for $BaTiO_3/CoFe_2O_4$ nanoparticles dispersed in PVDF membrane.

crystallinity of the final product has been increased as compared to the initial powder mixture. Crystallite size (D) in the mixture (before and after combustion) was estimated by using Scherrer's formula [31]: $D = \frac{k\lambda}{\beta cos\theta}$, where k is the constant (k = 0.94), λ is the wavelength of the X-ray, θ is Bragg's diffraction angle and β is the corrected full width of half maximum (FWHM) in radian of the selected peak, which is defined by$\beta = \beta_m^2 - \beta_s^2$, where β_m is the measured half-width of the sample and β_s is half-with of the standard reference material measured at the same angle.

To estimate the instrumental broadening(β_s), standard corundum sample was used. Two peaks from each phase were selected for the calculation; (i) (110) peak at 31.6° for $BaTiO_3$ (ii) (311) peak at 35.6° for $CoFe_2O_4$. The results are summarized in Table 1. Both crystallite size of $BaTiO_3$ and $CoFe_2O_4$ were increased after the reaction.

Fig. 5a and b show SEM images of $BaTiO_3$ and $CoFe_2O_4$ nanoparticles that were used in this work. Based on SEM data, the average particle sizes were approximately 200 nm and 30 nm, respectively. During initial product mixing, the granules of reagents formed agglomerates with spherical shape of around 10 μm–60 μm. Fig. 5, c shows that these particles consist of closely packed $BaTiO_3$ flakes and $CoFe_2O_4$ particles

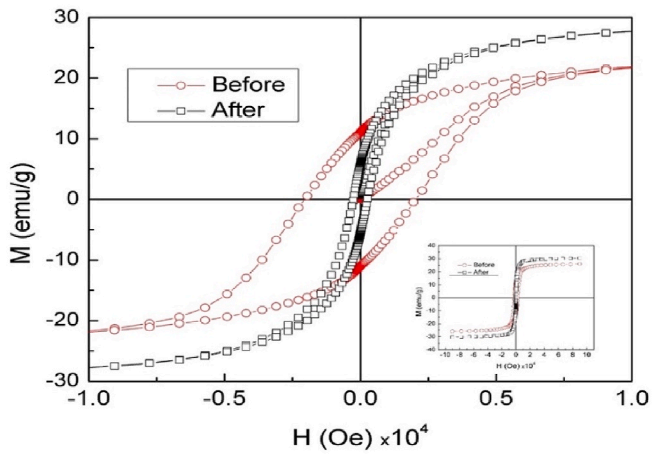

Fig. 9. Magnetization curves of $BaTiO_3/CoFe_2O_4$ initial and final composite, measured at T = 300 K (zoomed in). Insert is the full hysteresis loop at ± 9 T.

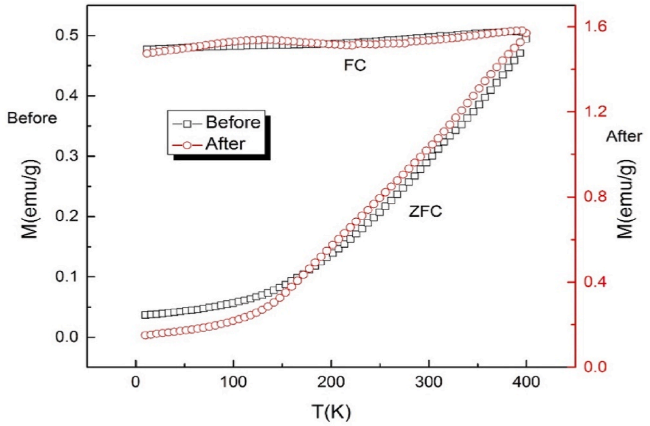

Fig. 10. Temperature dependence of magnetization curves of $BaTiO_3/CoFe_2O_4$ initial (black squere) and final composite (red circles) at magnetic field of H = 100 Oe.

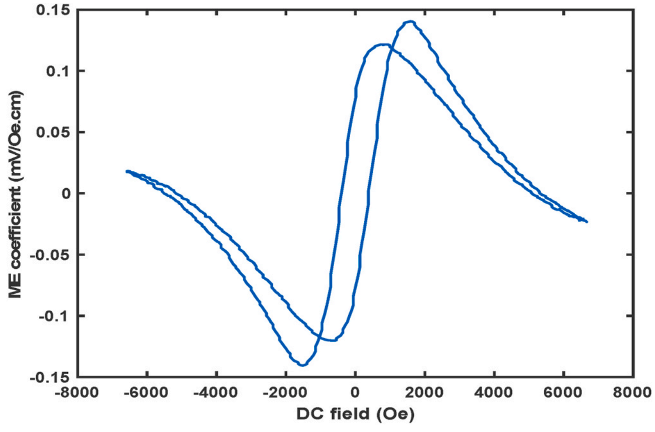

Fig. 11. Magnetoelectric coefficient of $BaTiO_3/CoFe_2O_4$ as a function of external DC magnetic field.

randomly distributed throughout the mixture. Fig. 5, d shows the SEM images of sample after the reaction, showing sintering of nanoparticles to each other to form Janus-like particles.

Although the combustion temperature during CCSO does not reach the adiabatic temperature values reported in Fig. 1, possible formation of hot-spots at the interfaces of particles create localized melting spots for formation of liquid phases described in the analysis of Fig. 1 and connecting the particles at these junction points. When the images are compared, it is evident that size of the flakes after the reaction were slightly increased as predicted by XRD calculations.

The end product is a nanocomposite of interconnected $BaTiO_3$ and $CoFe_2O_4$ particles (Fig. 6, a) sintered to each other. The SEM image of the FIB lamella (Fig. 6, b) shows the structure of the nanocomposite material. STEM-EDX mapping (Fig. 6, c) of the FIB lamella shows the distribution of elements throughout the sample.

The overlaid Ba and Fe EDX maps show the interconnected structure of the $BaTiO_3$ and $CoFe_2O_4$. STEM-EDX analysis of the sample (Fig. 7) shows that the $BaTiO_3$ and $CoFe_2O_4$ crystals are well sintered, and form agglomerates also observed in SEM.

Fig. 8 shows the surface potential for the $BaTiO_3/CoFe_2O_4$ nanoparticles dispersed in PVDF membrane and placed on gold plated silicon surface. Under the magnetic field, the surface potential decreases from about 140 mV (Fig. 8, b) to around 110 mV (Fig. 8, c). Thus, the magnetic field rearranges the domains and causes the powder to become better electrical conductor than in the absence of magnetic field, with over 20% difference between the surface potential values.

Fig. 9 shows initial and final magnetic hysteresis loops of the $BaTiO_3/CoFe_2O_4$ composite measured with a vibrating sample magnetometer with external magnetic field applied up to 9T. The hysteresis loops indicate the dependence of magnetization(M) on the applied magnetic field (H). Saturation magnetization was obtained from the relationship $M(H) = M_S(1\text{-}\beta/H)$, where β is a field independent parameter, Ms is saturation magnetization and H is the external field applied. Ms was estimated by extrapolating to zero field of the experimental M (H) curve from the high magnetic field range. Magnetization values are normalized with respect to the overall sample weight (both $BaTiO_3$ and $CoFe_2O_4$), rather than the amount of the $CoFe_2O_4$, where the major contributor for the hysteresis curve.

The value of saturation magnetization increases from 26.8 emu/g to 31.5 emu/g while coercivity decreases 2000 Oe to 250 Oe after the combustion. Since the coercivity depends on material microstructure, the observed decrease is both due to the grain growth and the grain morphology change resulting the change of magnetization switching dynamics.

Furthermore, noncollinear magnetic structure and surface effects can contribute to the increase of saturation magnetization and coercitive force. Temperature dependence of magnetization curves (Fig. 10) suggest that particles are of typical ferromagnetic nature. Since there are no major difference of the shape of the both initial and final graphs except magnetization of final product shows higher values, it can be concluded that there were no composition or structural changes introduced during the combustion. Higher values of M for final product can be attributed to the increased particle size. Further investigation of ZFC and FC curves show that there is a small kink in FC curve at 395 K, which is likely due to ferroelectric phase transition (Curie temperature) of $BaTiO_3$ where pyroelectric cubic phase transforms into tetragonal modification.

The results of magnetoelectric coefficient measurements are shown in Fig. 11. The data further affirm that the prepared composites indeed exhibit magnetoelectric properties. The highest ME coefficient observed at DC magnetic field of 1580 Oe is 0.14 mV/Oe-cm. The ME curve manifests a hysteretic behavior which originates from the hysteretic behavior of CFO component. Strictly speaking, the strain curve with respect to the DC magnetic field indicates hysteresis which is consequently transferred to the piezo magnetic and magnetoelectric curves as well. As a result, two peaks at different dc magnetic fields are distinctly observed. As the field increases (both in negative and positive directions) the ME coefficient indicates higher value relative to the situation where the field decreases. Moreover, the ME coupling coefficient demonstrates remanence which has roots in the remanence of polarization loop of BTO and charge accumulation in the grain boundaries [26]. A few articles have also reported the observation of hysteresis and remanence in CFO/BTO magnetoelectric composites [27,32].

3. Conclusions

The motivation of this study was to test a feasibility of synthesizing multiferroic $BaTiO_3$–$CoFe_2O_4$ Janus-like particles matrix structure by using CCSO. The major parameters affecting the process and product properties are the carbon concentration in the reactant mixture and the oxygen flow rate. The thermodynamic calculations as well as experimental work suggest that the mixture containing 5–10 wt % carbon should generate liquid phases which can help sintering the particles to form Janus-like structures. The initial mixture containing 10 wt % carbon is highly exothermic with 1430 J/g energy release and has activation energy ~112 kJ/mol. After the combustion, the crystallinity of product increases and the SEM, TEM and EDX mapping shows that the nanoparticles are sintered to each other. The AFM measurements show that the particles under magnetic field become better electrical conductors. The saturation magnetization is increased, while the coercivity is decreased after sintering. ZFC and FC measurements shows that there is a magnetoelectric coupling, suggesting that multiferroic $BaTiO_3$–$CoFe_2O_4$ composite can be synthesized by CCSO. Magnetoelectric coupling is further confirmed by direct measurement of the magnetoelectric coefficient of pallets formed from the CCSO product under application of external magnetic field. The highest magnetoelectric coefficient observed was 0.14 mV/Oe-cm.

Declaration of competing interest

The authors declare that they have no known competing financial interests or personal relationships that could have appeared to influence the work reported in this paper.

Acknowledgement

We would like to acknowledge the financial support for this research by National Science Foundation (NSF) PREM (award DMR-1523577: UTRGV-UMN Partnership for Fostering Innovation by Bridging Excellence in Research and Student Success) and NSF CBET-1928334 grant. J. T.H. and K.A.M. acknowledge support from the NSF MRSEC program under Awards DMR-1420013 and DMR-2011401. STEM analysis was performed in the Characterization Facility of the University of Minnesota, which receives partial support from the NSF through the MRSEC program.

References

[1] M. Nair, R. Guduru, P. Liang, J. Hong, V. Sagar, S. Khizroev, Externally controlled on-demand release of anti-HIV drug using magneto-electric nanoparticles as carriers, Nat. Commun. (2013), https://doi.org/10.1038/ncomms2717.

[2] S. Betal, A.K. Saha, E. Ortega, M. Dutta, A.K. Ramasubramanian, A.S. Bhalla, R. Guo, Core-shell magnetoelectric nanorobot - a remotely controlled probe for targeted cell manipulation, Sci. Rep. (2018), https://doi.org/10.1038/s41598-018-20191-w.

[3] R.E. Lu, K.G. Chang, B. Fu, Y.J. Shen, M.W. Xu, S. Yang, X.P. Song, M. Liu, Y. D. Yang, Magnetic properties of different $CoFe_2O_4$ nanostructures: nanofibers versus nanoparticles, J. Mater. Chem. C. (2014), https://doi.org/10.1039/c4tc01415d.

[4] C. Schmitz-Antoniak, D. Schmitz, P. Borisov, F.M.F. De Groot, S. Stienen, A. Warland, B. Krumme, R. Feyerherm, E. Dudzik, W. Kleemann, H. Wende, Electric in-plane polarization in multiferroic $CoFe_2O$ $_4$/$BaTiO_3$ nanocomposite tuned by magnetic fields, Nat. Commun. (2013), https://doi.org/10.1038/ncomms3051.

[5] H. Zheng, J. Wang, S.E. Lofland, Z. Ma, L. Mohaddes-Ardabili, T. Zhao, L. Salamanca-Riba, S.R. Shinde, S.B. Ogale, F. Bai, D. Viehland, Y. Jia, D.G. Schlom, M. Wuttig, A. Roytburd, R. Ramesh, Multiferroic $BaTiO_3$-$CoFe_2O_4$ nanostructures, Science 80 (2004), https://doi.org/10.1126/science.1094207.

[6] S. Haffer, C. Lüder, T. Walther, R. Köferstein, S.G. Ebbinghaus, M. Tiemann, A synthesis concept for a nanostructured $CoFe_2O_4$/$BaTiO_3$ composite: towards multiferroics, Microporous Mesoporous Mater. (2014), https://doi.org/10.1016/j.micromeso.2014.05.023.

[7] T. Walther, U. Straube, R. Köferstein, S.G. Ebbinghaus, Hysteretic magnetoelectric behavior of CoFe2O4-BaTiO3 composites prepared by reductive sintering and reoxidation, J. Mater. Chem. C. (2016), https://doi.org/10.1039/c6tc00995f.

[8] B. Fu, R. Lu, K. Gao, Y. Yang, Y. Wang, Magnetoelectric coupling in multiferroic $BaTiO_3$-$CoFe_2O_4$ composite nanofibers via electrospinning, EPL, 2015, https://doi.org/10.1209/0295-5075/111/17007.

[9] V. Corral-Flores, D. Bueno-Baqués, R.F. Ziolo, Synthesis and characterization of novel $CoFe_2O_4$-$BaTiO_3$ multiferroic core-shell-type nanostructures, Acta Mater. (2010), https://doi.org/10.1016/j.actamat.2009.09.054.

[10] G.V. Duong, R. Groessinger, R. Sato Turtelli, Effect of structure on magnetoelectric properties of $CoFe_2O_4$-$BaTiO_3$ multiferroic composites, J. Magn. Magn Mater. (2007), https://doi.org/10.1016/j.jmmm.2006.10.338.

[11] G.V. Duong, R. Groessinger, Effect of preparation conditions on magnetoelectric properties of $CoFe_2O_4$-$BaTiO_3$ magnetoelectric composites, J. Magn. Magn Mater. (2007), https://doi.org/10.1016/j.jmmm.2007.03.142.

[12] A. Chaudhuri, K. Mandal, Large magnetoelectric properties in $CoFe_2O_4$:$BaTiO_3$ core-shell nanocomposites, J. Magn. Magn Mater. (2015), https://doi.org/10.1016/j.jmmm.2014.10.142.

[13] M.M. Selvi, P. Manimuthu, K.S. Kumar, C. Venkateswaran, Magnetodielectric properties of $CoFe_2O_4$-$BaTiO_3$ core-shell nanocomposite, J. Magn. Magn Mater. (2014), https://doi.org/10.1016/j.jmmm.2014.06.039.

[14] T. Nisisako, T. Torii, T. Takahashi, Y. Takizawa, Synthesis of monodisperse bicolored janus particles with electrical anisotropy using a microfluidic co-flow system, Adv. Mater. (2006), https://doi.org/10.1002/adma.200502431.

[15] D. Rodríguez-Fernández, L.M. Liz-Marzán, Metallic Janus and patchy particles, Part. Part. Syst. Char. (2013), https://doi.org/10.1002/ppsc.201200057.

[16] G.A. Sotiriou, A.M. Hirt, P.Y. Lozach, A. Teleki, F. Krumeich, S.E. Pratsinis, Hybrid, silica-coated, Janus-like plasmonic-magnetic nanoparticles, Chem. Mater. (2011), https://doi.org/10.1021/cm200399t.

[17] K.S. Martirosyan, D. Luss, Carbon combustion synthesis of oxides, US Patent 7 (135) (2011) 897.

[18] K.S. Martirosyan, D. Luss, Carbon combustion synthesis of complex oxides: process demonstration and features, AIChE J. (2005), https://doi.org/10.1002/aic.10528.

[19] K.S. Martirosyan, D. Luss, Carbon combustion synthesis of Ferrites: synthesis and characterization, Ind. Eng. Chem. Res. 46 (2007) 1492, https://doi.org/10.1021/ie060571l.

[20] K.S. Martirosyan, L. Chang, J. Rantschler, S. Khizroev, D. Luss, D. Litvinov, Carbon combustion synthesis and magnetic properties of cobalt ferrite nanoparticles, IEEE Trans. Magn. 43 (6) (2007) 3118, https://doi.org/10.1109/TMAG.2007.893844.

[21] K.S. Martirosyan, E. Galstyan, S.M. Hossain, Y.J. Wang, D. Litvinov, Barium hexaferrite nanoparticles: synthesis and magnetic properties, mater. Sci. Eng. B solid-state mater, Adv. Met. Technol. (2011), https://doi.org/10.1016/j.mseb.2010.08.005.

[22] K.S. Martirosyan, C. Dannangoda, E. Galstyan, D. Litvinov, Screen-printing of ferrite magnetic nanoparticles produced by carbon combustion synthesis of oxides, J. Appl. Phys. (2012), https://doi.org/10.1063/1.4711097.

[23] W. Greiner, L. Neise, H. Stöcker, Thermodynamics and Statistical Mechanics, 1995, https://doi.org/10.1007/978-1-4612-0827-3.

[24] A.A. Shiryaev, Thermodynamics of SHS processes: advanced approach, Int. J. Self-Propag. High-Temp. Synth. (1995), https://doi.org/10.1017/CBO9781107415324.004.

[25] A. Varma, A.S. Rogachev, A.S. Mukasyan, S. Hwang, Combustion synthesis of advanced materials: principles and applications, Adv. Chem. Eng. (1998), https://doi.org/10.1016/S0065-2377(08)60093-9.

[26] G.V. Duong, R. Groessinger, Effect of preparation conditions on magnetoelectric properties of $CoFe_2O_4$-$BaTiO_3$ magnetoelectric composites, J. Magn. Magn Mater. (2007), https://doi.org/10.1016/j.jmmm.2007.03.142.

[27] G.V. Duong, R. Groessinger, M. Schoenhart, D. Bueno-Basques, The lock-in technique for studying magnetoelectric effect, J. Magn. Magn Mater. (2007), https://doi.org/10.1016/j.jmmm.2007.03.185.

[28] M.J. Starink, The determination of activation energy from linear heating rate experiments: a comparison of the accuracy of isoconversion methods, Thermochim. Acta (2003), https://doi.org/10.1016/S0040-6031(03)00144-8.

[29] H.E. Kissinger, Reaction kinetics in differential thermal analysis, Anal. Chem. (1957), https://doi.org/10.1021/ac60131a045.

[30] T. Ozawa, Kinetic analysis of derivative curves in thermal analysis, J. Therm. Anal. (1970), https://doi.org/10.1007/BF01911411.

[31] J.I. Langford, A.J.C. Wilson, Scherrer after sixty years: a survey and some new results in the determination of crystallite size, J. Appl. Crystallogr. (1978), https://doi.org/10.1107/s0021889878012844.

[32] T. Walther, U. Straube, R. Köferstein, S.G. Ebbinghaus, Hysteretic magnetoelectric behavior of CoFe2O4-BaTiO3 composites prepared by reductive sintering and reoxidation, J. Mater. Chem. C. (2016), https://doi.org/10.1039/c6tc00995f.